









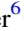




## Cloud Atlas: Discovery of Rotational Spectral Modulations in a Low-mass, L-type Brown Dwarf Companion to a Star

Item Type	Article
Authors	Manjavacas, Elena; Apai, Dániel; Zhou, Yifan; Karalidi, Theodora; Lew, Ben W. P.; Schneider, Glenn; Cowan, Nicolas B.; Metchev, Stanimir A.; Miles-Páez, Paulo A.; Burgasser, Adam J.; Radigan, Jacqueline; Bedin, Luigi R.; Lowrance, Patrick J.; Marley, Mark S.
Citation	Cloud Atlas: Discovery of Rotational Spectral Modulations in a Low-mass, L-type Brown Dwarf Companion to a Star 2017, 155 (1):11 The Astronomical Journal
DOI	<a href="https://doi.org/10.3847/1538-3881/aa984f">10.3847/1538-3881/aa984f</a>
Publisher	IOP PUBLISHING LTD
Journal	The Astronomical Journal
Rights	© 2017. The American Astronomical Society. All rights reserved.
Download date	26/08/2022 18:14:50
Item License	<a href="http://rightsstatements.org/vocab/InC/1.0/">http://rightsstatements.org/vocab/InC/1.0/</a>
Version	Final published version
Link to Item	<a href="http://hdl.handle.net/10150/626404">http://hdl.handle.net/10150/626404</a>



# Cloud Atlas: Discovery of Rotational Spectral Modulations in a Low-mass, L-type Brown Dwarf Companion to a Star

Elena Manjavacas<sup>1</sup>, Dániel Apai<sup>1,2,11</sup> , Yifan Zhou<sup>1</sup> , Theodora Karalidi<sup>1,3</sup> , Ben W. P. Lew<sup>2</sup> , Glenn Schneider<sup>1</sup> ,  
Nicolas Cowan<sup>4</sup> , Stan Metchev<sup>5</sup> , Paulo A. Miles-Páez<sup>1,5</sup> , Adam J. Burgasser<sup>6</sup> , Jacqueline Radigan<sup>7</sup>,  
Luigi R. Bedin<sup>8</sup>, Patrick J. Lowrance<sup>9</sup> , and Mark S. Marley<sup>10</sup> 

<sup>1</sup> Department of Astronomy/Steward Observatory, The University of Arizona, 933 N. Cherry Avenue, Tucson, AZ 85721, USA; [elenamanjavacas@email.arizona.edu](mailto:elenamanjavacas@email.arizona.edu)

<sup>2</sup> Department of Planetary Science/Lunar and Planetary Laboratory, The University of Arizona, 1640 E. University Boulevard, Tucson, AZ 85718, USA

<sup>3</sup> Department of Astronomy and Astrophysics, University of California, Santa Cruz, California, USA

<sup>4</sup> Department of Earth & Planetary Sciences, 3450 University St. Montreal, Quebec H3A 0E8, Canada

<sup>5</sup> The University of Western Ontario, Department of Physics and Astronomy, 1151 Richmond Avenue, London, ON N6A 3K7, Canada

<sup>6</sup> Center for Astrophysics and Space Science, University of California San Diego, La Jolla, CA 92093, USA

<sup>7</sup> Utah Valley University, 800 West University Parkway, Orem, UT 84058, USA

<sup>8</sup> INAF—Osservatorio Astronomico di Padova, Vicolo dell'Osservatorio 5, I-35122 Padova, Italy

<sup>9</sup> IPAC-Spitzer, MC 314-6, California Institute of Technology, Pasadena, CA 91125, USA

<sup>10</sup> NASA Ames Research Center, Mail Stop 245-3, Moffett Field, CA 94035, USA

Received 2017 August 10; revised 2017 October 20; accepted 2017 October 22; published 2017 December 12

## Abstract

Observations of rotational modulations of brown dwarfs and giant exoplanets allow the characterization of condensate cloud properties. As of now, rotational spectral modulations have only been seen in three L-type brown dwarfs. We report here the discovery of rotational spectral modulations in LP261-75B, an L6-type intermediate surface gravity companion to an M4.5 star. As a part of the *Cloud Atlas* Treasury program, we acquired time-resolved Wide Field Camera 3 grism spectroscopy (1.1–1.69  $\mu\text{m}$ ) of LP261-75B. We find gray spectral variations with the relative amplitude displaying only a weak wavelength dependence and no evidence for lower-amplitude modulations in the 1.4  $\mu\text{m}$  water band than in the adjacent continuum. The likely rotational modulation period is  $4.78 \pm 0.95$  hr, although the rotational phase is not well sampled. The minimum relative amplitude in the white light curve measured over the whole wavelength range is  $2.41\% \pm 0.14\%$ . We report an unusual light curve, which seems to have three peaks approximately evenly distributed in rotational phase. The spectral modulations suggests that the upper atmosphere cloud properties in LP261-75B are similar to two other mid-L dwarfs of typical infrared colors, but differ from that of the extremely red L-dwarf WISE0047.

*Key words:* brown dwarfs – stars: atmospheres

## 1. Introduction

Brown dwarfs and giant non-irradiated exoplanets of younger ages share similar ranges of temperatures and atmospheric abundances and have similar spectra, which are influenced by condensate clouds that are common in their atmospheres (Reid et al. 2008; Cruz et al. 2009; Kirkpatrick et al. 2010; Faherty et al. 2013, and references therein). Due to these similarities, comparative studies of brown dwarfs and giant exoplanets provide powerful insights into the atmospheric structures and processes common to these objects.

In addition, solar system giant planets—that can be studied at great detail—provide cooler and lower-mass analogs to brown dwarfs that help us understand the dynamics, composition, and structures in brown dwarf and exoplanet atmospheres. Giant planets in our solar system show bands, hot spots, zones, jets, and storms that vary over time. Ackerman & Marley (2001) suggested that similar heterogeneous cloud patterns and structures may be inferred also in brown dwarfs, resulting in photometric variability driven by the cloud structures in brown dwarf atmospheres. Rotational modulations due to heterogeneous clouds have been observed in Jupiter’s light curve; Karalidi et al. (2015) measured *U*- and *R*-band rotational

modulations. They compared them with simultaneous *Hubble Space Telescope* (*HST*) images, showing that hot spots in the atmosphere of Jupiter are responsible for its troughs in the light curve, and the Great Red Spot is responsible for the peaks. In addition, Simon et al. (2016) carried out a similar study on Neptune using *Kepler* data and disk-resolved images from the *Keck* 10 m telescope, obtaining analogous results.

Putative photometric variability for brown dwarfs (Bailer-Jones & Mundt 1999, 2001; Tinney & Tolley 1999; Gelino et al. 2002; Koen 2003; Morales-Calderón et al. 2006, and references therein) had also been reported almost since their discovery. Most likely, the first robust and confirmed variability detection due to heterogeneous cloud coverage in the atmosphere of a brown dwarf is from Artigau et al. (2009), for 2MASS J0136565+093347 (SIMP0136). Multiple analyses show that photometric variability of brown dwarfs older than 10 Myr and with spectral types later than L3 is most likely due to heterogeneous cloud coverage (Artigau et al. 2009; Radigan et al. 2012; Apai et al. 2013; Buenzli et al. 2015; Metchev et al. 2015). These conclusions are supported by the lack of correlation between  $H\alpha$  emission and variability. This strongly suggests that magnetically induced spots (starspots) are not responsible for photometric variability in most brown dwarfs (Miles-Páez et al. 2017). In addition, because dust grains coagulate rapidly in brown dwarf disks (Apai et al. 2005;

<sup>11</sup> Earths in Other Solar Systems Team, NASA Nexus for Exoplanet System Science.

Pascucci et al. 2009) and the typical lifetimes of optically thick dust disks around brown dwarfs is less than 10 Myr (Carpenter et al. 2006), remnant dust disks also cannot be the primary source of variability. Indeed, Radigan et al. (2012) compared time-resolved near-infrared photometric data to Saumon & Marley (2008) atmospheric models for cloudy atmospheres with different cloud thickness, finding that models could only reproduce the overall shape of the (time-averaged) spectrum and the ratio of photometric variability amplitudes for the L/T transition brown dwarf 2MASS J21392676+0220226 (2M2139), with changes in *both* the surface temperature and cloud coverage. They demonstrated that the photometric variability of 2M2139 originated from patchy cloud coverage: either from holes or cloud thickness variations. Apai et al. (2013) presented time-resolved *HST* near-infrared spectra and studied photometric and spectral variations, showing that the variability in two L/T transition brown dwarfs (2M2139 and SIMP0136) is caused by correlated cloud thickness and temperature variations. In 2014, Buenzli et al. (2014) modeled near-infrared spectral variations observed in Luhman 16B with *HST* and confirmed that the variability in this L/T transition object is also explained by correlated cloud thickness and temperature variations.

Non-axisymmetric cloud structures in a rotating ultracool atmosphere introduce distinct signatures in their disk-integrated light curves. An observed light curve is a geometrically weighted, observable-disk-integrated function of the surface brightness distribution of the target (Cowan & Agol 2008; Cowan et al. 2017). As the source rotates, the projected position of cloud structures on the observable hemisphere changes, altering its disk-integrated intensity. By modeling the observed light curve, we can place constraints on the properties of the cloud structures, such as their location on the disk (longitude, latitude), size, and contrast to the background atmosphere (Knutson et al. 2007; Apai et al. 2013; Cowan et al. 2013; Karalidi et al. 2015).

To date, published light curves of various ultracool dwarfs show single or double peaks, whose shapes vary with time, sometimes even within a single rotation (Artigau et al. 2009; Radigan et al. 2012; Apai et al. 2013; Gillon et al. 2013; Buenzli et al. 2015; Karalidi et al. 2015; Metchev et al. 2015; Lew et al. 2016; Yang et al. 2016). These observations are interpreted as single or multiple cloud structures in the atmosphere of brown dwarfs that can evolve at short timescales. Based on a comprehensive *Spitzer Space Telescope* photometric monitoring program, Apai et al. (2017) reported dramatic and continuous light-curve evolution in six brown dwarfs, all of which showed a quasi-periodic light curve. For three of the targets—all at the L/T transition—they found that two or three planetary-scale waves ( $k = 1$  and  $k = 2$  waves, where  $k$  is the wavenumber) provided good fits to the light curves, if the  $k = 1$  waves had similar, but slightly different periods. These slightly different peaks in the power spectrum could be attributed to differential rotation, although that explanation is not unique. These results argue for zonal atmospheric circulation and planetary-scale waves in L/T transition brown dwarfs.

In this paper, we present, analyze, and discuss the unusual light curve of LP261-75B (L6 brown dwarf companion to a M4.5 star) with hints of three peaks. In Section 2, we describe the characteristics of LP261-75B. In Section 3, we describe the observations acquired and the data reduction performed. In Section 4, we present the analysis we performed to rule out the possibility that systematics are influencing our results. In Section 5, we analyze the possible causes that would explain the spectro-photometric variability of LP261-75B. In Section 6,

we summarize the results obtained from the analysis of the spectroscopy and light curves of LP261-75B. In Section 7, we examine the possible causes that could explain the unusual light curve of the object. Finally, we summarize our conclusions in Section 8.

## 2. LP261-75B

2MASSW J09510549+3558021 was discovered by Kirkpatrick et al. (2000). 2MASSW J09510549+3558021 has an L6 spectral type in the optical (Kirkpatrick et al. 2000), and an L4.5 spectral type in the near-infrared (Allers & Liu 2007). Its *J*-, *H*-, and *K*-band magnitudes of  $17.23 \pm 0.21$ ,  $15.89 \pm 0.14$  and  $15.14 \pm 0.14$ , respectively. Burgasser et al. (2005) discovered that 2MASSW J09510549+3558021 (LP261-75B) is a companion of the LP261-75A active M4.5 star, with a separation of  $12''$ . The system is at a trigonometric distance of  $31.6 \pm 1.3$  pc (Liu et al. 2016).

Reid & Walkowicz (2006) estimated an age of 100–300 Myr for LP261-75A based on its coronal activity levels, which are comparable to stars with similar spectral types in the Pleiades open cluster (of age  $125 \pm 8$  Myr, Stauffer et al. 1998). Shkolnik et al. (2009) estimated an age between 40 and 300 Myr through the X-ray activity of LP261-75A. Assuming an average age for LP261-75AB of 100–200 Myr, evolutionary models (Burrows et al. 2001) provide an estimated mass for LP261-75B between 15 and  $30 M_{\text{Jup}}$  (Artigau et al. 2015).

LP261-75B’s spectral energy distribution is similar to those typical to field L6 brown dwarfs, with similarly prominent FeH features in the *H*-band, and alkali lines in the near-infrared spectra (Liu et al. 2016). These spectral characteristics are consistent with those expected for an L6 brown dwarf with an age at the upper end of the given age range for LP261-75B (40–300 Myr, Stauffer et al. 1998)

## 3. Observations and Data Reduction

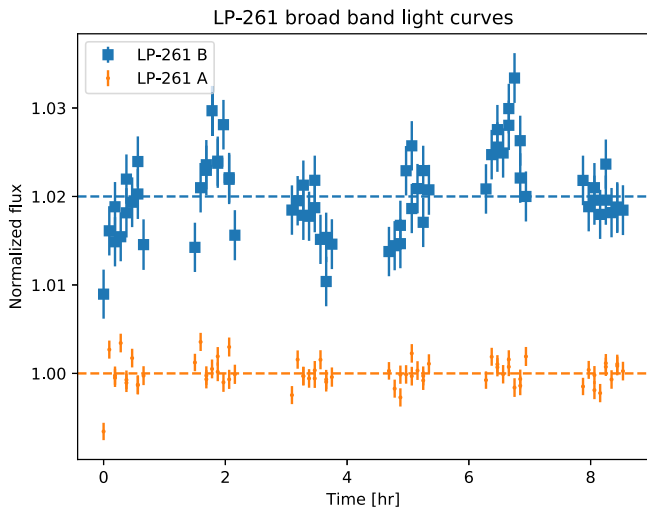
LP261-75B was observed in Cycle 23 of the *HST* program (P.I. D. Apai, GO14241) using the Wide Field Camera 3 (WFC3) in the near-infrared channel, and its G141 grism (MacKenty et al. 2010). WFC3 with the G141 grism covers the wavelength range between  $\sim 1.05$  and  $1.7 \mu\text{m}$ , with a spectral resolving power of 130 at  $1.4 \mu\text{m}$ . WFC3/IR has a plate scale of 0.13 arcsec/pixel. We acquired six consecutive orbits of observations on 2016 December 21, UTC. To obtain an accurate wavelength reference, a direct image in each orbit was also taken in the F132N filter. We used a  $256 \times 256$  subarray mode to eliminate mid-orbit buffer dumps.

We performed the data reduction using the same method as in previous works published by our group (Apai et al. 2013; Buenzli et al. 2014; Yang et al. 2015; Lew et al. 2016). The uncertainty level for our spectra after the data reduction is 0.1%–0.3% per spectral bin, measured using the reduced spectra in the range of  $1.1$ – $1.69 \mu\text{m}$  to avoid the noise at the edges of the spectra due to the drop in the instrument sensitivity. These uncertainties are due to photon noise, errors in the sky subtraction, and the read-out noise.

## 4. Systematics Corrections

### 4.1. Aperture Selection

Due to the close angular proximity of the bright M4.5 star (LP261-75A), care must be taken when choosing the spectral



**Figure 1.** Broad-band or white light curves (1.1–1.69  $\mu\text{m}$ ) of LP261-75B (blue dots) and LP261-75A (orange dots). The fluxes of the light curves are normalized to their respective mean fluxes. We applied a positive shift in the y-axis to the LP261-75B light curve to overplot both light curves in the same plot.

extraction rectangular aperture, parallel to the direction. If the spectral extraction aperture is too wide, the spectra of LP261-75B may be contaminated by the spectra of the primary; if the aperture is too narrow, the signal-to-noise will be compromised. To explore the effect of the aperture width choice, we have performed the data reduction using apertures ranging from 0.5 to  $20 \times \text{FWHM}$  (Full Width at Half Maximum), with steps of 0.5 FWHM (measured in pixels), at 1.4  $\mu\text{m}$  centered at the position of the target spectrum. We measured the total flux of the spectrum for each of those apertures. In the explored aperture width range we did not see an inflection in the flux that would have indicated measurable contamination from the primary up to apertures bigger than  $18 \times \text{FWHM}$ ; the lack of this contamination was in line with the separation of the primary and with the outcome of our contamination tests. We chose the smallest aperture (7 FWHM) for which the difference of flux between incrementally larger apertures was below 1%, indicating that the aperture is capturing most of the intensity in the line spread function.

In Figure 1, we show the resulting broad-band light curves for LP261-75A and LP261-75B.

#### 4.2. Pointing Stability

Our flux density measurements might be also influenced by the pointing stability of the instrument plus the telescope system within a given orbit. To assess the magnitude of this effect, we measured the central positions of the spectra in each exposure in all six orbits, fitting a Gaussian function to the spatial direction in six different columns. We concluded that the pointing jitter and/or drift of *HST* was about one-tenth of a pixel or less within each of the six orbits (much smaller than the aperture size we adopted). Therefore, the pointing drift or jitter does not affect significantly our measurements.

#### 4.3. Ramp Correction

The most prominent source of systematics on WFC3/IR data is the “ramp effect,” which consists of an approximately exponential-shape signal that increases with time during every orbit. The correction described in Zhou et al. (2017) models the

charge trapping process of WFC3 infrared detector and calculates a ramp effect systematic light curve, which is used to recover the intrinsic signal. Each photometric data point was corrected for the ramp effect considering the entire data set (all data points in every orbit) using the physically motivated detector charge trap model developed by Zhou et al. (2017). This approach models the number of charges trapped in a given pixel and their delayed release, allowing for the correction of every orbit (including the first), reducing the ramp effects amplitude by at least an order of magnitude. After this correction, the dominant source of noise in our data is the photon noise.

#### 4.4. Sky Background

We tested the possibility that time-varying scattered light would affect the light curve we obtained for LP261-75B. To rule out that option, we measured the values of the sky after sky background subtraction, and ramp correction, in four different regions of  $256 \times 30$  pixels in the detector. The chosen regions span from pixels  $y = 87\text{--}117$  (region 1),  $y = 117\text{--}147$  (region 2), and pixels  $y = 162\text{--}192$  (region 3) and  $y = 192\text{--}222$  (region 4), avoiding the areas between pixels  $y = 0\text{--}87$ , and pixels  $y = 147\text{--}162$ , where the spectra of LP261A and LP261-75B were located.

We calculated the Kendall’s  $\tau$  coefficient to investigate a potential correlation between the variations of the sky background after ramp correction and sky subtraction, and the ramp-corrected white light curve of LP261-75B for the four selected regions. We obtained Kendall coefficients close to 0 (region 1:  $\tau = -0.15$ , significance: 0.08; region 2:  $\tau = -0.13$ , significance = 0.12; region 3:  $\tau = -0.16$ , significance: 0.056; region 4:  $\tau = 0.08$ , significance = 0.37), indicating no correlation. Therefore, we conclude that slight variations in the sky background do not influence measurably the light curve of our target.

#### 4.5. Correlation between LP261-75A and B Light Curves

Finally, we searched for correlations between the normalized light curves of LP261-75A and LP261-75B after their respective ramp corrections, performed as indicated in Section 4.3. We calculated Kendall correlation coefficients between their white light curves, obtaining a Kendall’s  $\tau$  coefficient close to 0 ( $\tau = 0.03$ , significance: 0.73), indicating no correlation between LP261-75A and LP261-75B light curves. Therefore, we conclude that any potential variations in the measured brightness of LP261-75A do not influence the light curve we measured for LP261-75B, i.e., the variations seen in LP261-75B are intrinsic.

### 5. Origin of the Spectro-photometric Variability of LP261-75B

In this section, we evaluate the possible causes that would explain the spectro-photometric variability found for a mid-L dwarf as LP261-75B.

1. *Binarity.* Our *HST* wavelength calibration (direct) images do not resolve any companion to LP261-75B itself at a separation higher than  $\sim 1.25$  AU. In case LP261-75B is an unresolved binary system, we would expect it to be overluminous in a color–magnitude diagram in comparison to its counterparts of similar spectral type. For LP261-75B, its absolute magnitude ( $M_J$ ) in *J*-band is



$14.6 \pm 0.09$ , consistent with the absolute magnitude expected for a L7 dwarf (the spectro-photometric  $M_J$  for a L7 is  $14.3 \pm 0.4$ , using Dupuy & Liu (2012) spectro-photometric relation.) Therefore, we conclude that binarity is most probably not the cause of the variability in the light curve of LP261-75B.

2. *Magnetic spots.* In L-dwarfs, the magnetic Reynolds number, a parameter that describes how efficient a gas interacts with a magnetic field, is too small to support the formation of magnetic spots on L-dwarf atmospheres (Gelino et al. 2002). In addition, Miles-Páez et al. (2017) concluded that chromospheric activity and photometric variability are not correlated, specially for objects with spectral types later than L3.5. In the case of LP261-75B, no evidence of H- $\alpha$  emission has been found (Kirkpatrick et al. 2000), indicating a lack of magnetic activity. Therefore, we do not expect that the photometric variability found for LP261-75B is caused by magnetic spots.
3. *Heterogeneous cloud coverage.* Ackerman & Marley (2001) proposed that heterogeneous clouds similar to those found in the atmospheres of giant planets of our solar system may be present in the atmospheres of brown dwarfs as well. In fact, photometric variability has been observed for brown dwarfs from mid-L to the late-T spectral types (Artigau et al. 2009; Radigan et al. 2012; Apai et al. 2013; Buenzli et al. 2015; Metchev et al. 2015; Yang et al. 2015; Lew et al. 2016). Inhomogeneous cloud coverage has been found to be the most plausible cause of photometric variability in L/T transition brown dwarfs (Radigan et al. 2012; Apai et al. 2013). For the mid-L dwarfs, Yang et al. (2015) showed that their photometric variability could be due to high-altitude haze clouds above condensate clouds. Therefore, we conclude that the most plausible cause of spectro-photometric variability is the existence of heterogeneous cloud coverage in the atmosphere of LP261-75B.

## 6. Results

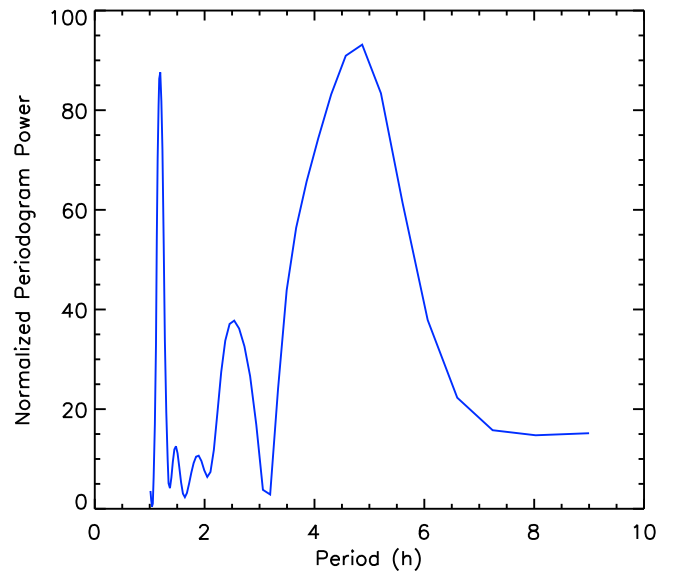
### 6.1. Rotational Period

#### 6.1.1. Lomb–Scargle Periodogram

We determined the rotational period through a periodogram using the `IDL@periodogram.pro` function. This routine employs the method described by Horne & Baliunas (1986), based on the Lomb–Scargle periodogram (Lomb 1976; Scargle 1982), to calculate a periodogram within user-set frequency or period limits for a time series of data. The data do not need to be equally spaced. The power obtained is normalized to the variance of the total data. The periodogram derived from the LP261-75B light curve (as shown in Figure 1) is illustrated in Figure 2. We retrieved a principal period of  $4.87 \pm 0.25$  hr and a shorter period of significance of  $1.19 \pm 0.01$  hr, with uncertainties as computed by Horne & Baliunas (1986; *ibid.*, c.f. their Equation (14)). The principal period is close to  $3 \times$  the *HST* orbit period of 1.59 hr), and the shorter periods are close (but not exactly equal) to harmonics of the principal period.

#### 6.1.2. Bayesian Generalized Lomb–Scargle (BGLS) Periodogram

The Lomb–Scargle periodogram does not take into account uncertainties in flux. The Lomb–Scargle periodogram fits a sine



**Figure 2.** Periodogram of the white light curve of LP261-75B. The maximum corresponds to the period of the light curve, which is  $4.87 \pm 0.25$  hr.

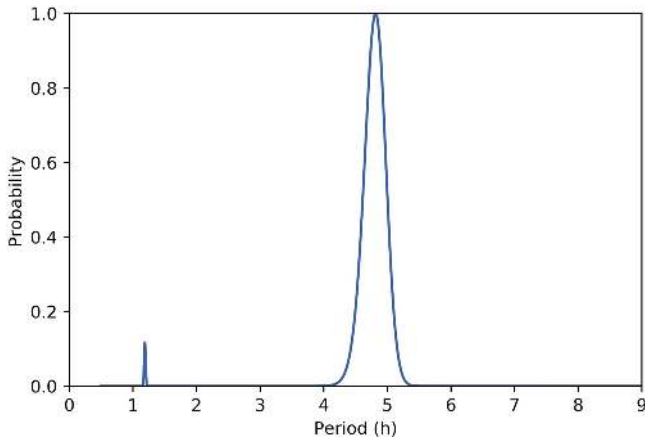
wave to the data to determine the most probable periods. However, it assumes that the mean of the data and the mean of the sine wave fitted to the data to obtain the most probable periods is the same. In addition, the Lomb–Scargle periodogram as presented in Section 6.1.1, is expressed in an arbitrary power. These deficiencies have been addressed by several authors (Ferraz-Mello 1981; Cumming et al. 1999; Bretthorst 2001; Zechmeister & Kürster 2009; Mortier et al. 2015). In addition, Cowan et al. (2017) concluded that the periodogram by Horne & Baliunas (1986) provide biased results in case of temporal gaps in the data.

Mortier et al. (2015)<sup>12</sup> provided a Python-based program to calculate the BGLS periodogram of time-series based on Bretthorst (2001) and Zechmeister & Kürster (2009). It provides the relative probabilities between different peaks of similar power in the LS periodogram, taking into account the uncertainties of the data, possible gaps, and any possible zero point difference in the data collected at different epochs. The periodogram is shown in Figure 3. We retrieved a principal period of  $4.78 \pm 0.37$  hr, and other shorter period of significance of  $1.19 \pm 0.04$  hr, with uncertainties as computed as the FWHM of each of the peaks after fitting a Gaussian to each of them.

#### 6.1.3. Fourier Function Fit

Recently, Apai et al. (2017) showed that light curve evolution observed in three L/T transition brown dwarfs with near-continuous *Spitzer Space Telescope* photometry were well-described by planetary-scale waves with periods similar to but slightly different from the likely rotational periods of the objects. This model successfully fitted the light curve evolution as  $k = 1$  and  $k = 2$  ( $k$ —wavenumber) waves. In the following, we also explore fitting the LP261-75B data with a Fourier series motivated by the results of Apai et al. (2017), without necessarily adopting the same interpretation.

<sup>12</sup> <https://www.astro.up.pt/exoearths/tools.html>



**Figure 3.** Bayesian generalized Lomb–Scargle periodogram of the white light curve of LP261-75B. The y-axis shows the probability that a signal with a specific period is present in the data. Probabilities are normalized to the probability of the highest peak. The period obtained for the light curve is  $4.78 \pm 0.37$  hr.

We fitted a 1–5 degree Fourier function fit to the white light curve using the following expression:

$$F(t) = \frac{A_0}{2} + \sum_{n=1}^{1 \text{ to } 5} \left[ A_n \cos\left(\frac{2\pi n}{P}t\right) + B_n \sin\left(\frac{2\pi n}{P}t\right) \right]. \quad (1)$$

We performed a Levenberg–Marquardt least-squares fit to the Fourier function, using the IDL function `mpfitfun.pro` (Markwardt 2009). We chose the fourth Fourier function as the best fit to the white light curve, as it gave the lowest reduced  $\chi^2$  ( $\chi_{\text{red}}^2 = 1.06$ ) and the lowest Bayesian Information Criterion (Liddle 2007, BIC). In Table 1, we summarize the values of the  $\chi_{\text{red}}^2$  and the BIC for each of the Fourier functions we fitted to the white light curve. For the smallest  $\chi_{\text{red}}^2$  and BIC fit, we obtained a period of  $4.76 \pm 0.03$  hr, in statistical agreement with the principal period determined from the two periodogram analysis. In Table 2, we show the values of the Fourier components calculated for the fourth-order Fourier fit. In Figure 4, top plots, we show the non-folded light curve on the left, and the phase-folded light curve on the right, using the result of the period found from the fourth-order Fourier fit. After phase-folding the white light curve, we retrieved a light curve with hints of three peaks. The residual of the best-fitting Fourier function was smaller than 0.1% in amplitude, that is of the order of magnitude of the uncertainty level per spectral bin (0.1%–0.3%; see Figure 4, bottom plots).

Although the principal periods retrieved by the three methods are in statistical agreement, it is important to note that after trying different sets of initial conditions, the Levenberg–Marquardt least-squares fit method only converged for a specific set of defined initial conditions.

#### 6.1.4. Robust Estimation of Periods and Uncertainties

Due to target visibility interruptions, our data do not sample, or closely flank, the troughs of the phase-folded light curve (Figure 4, top right panel). We thus present the subsequent analysis to robustly estimate the significant main periods and their uncertainties using different Monte Carlo simulations.

1. Regular Monte Carlo simulation: we generate 1000 synthetic light curves slightly different in flux values from the observed light curve by redefining each data

**Table 1**  
Reduced  $\chi^2$  and BIC (Bayesian Information Criterion) of the Fourier Functions Fitted to LP261-75B White Light Curve

Order of Fourier Fit	$\chi_{\text{red}}^2$	BIC
1st	1.67	128.8
2nd	1.69	126.6
3rd	1.24	105.8
4th	1.06	101.6
5th	1.10	109.9

**Table 2**  
Amplitudes for the Fourth-order Fourier Fit

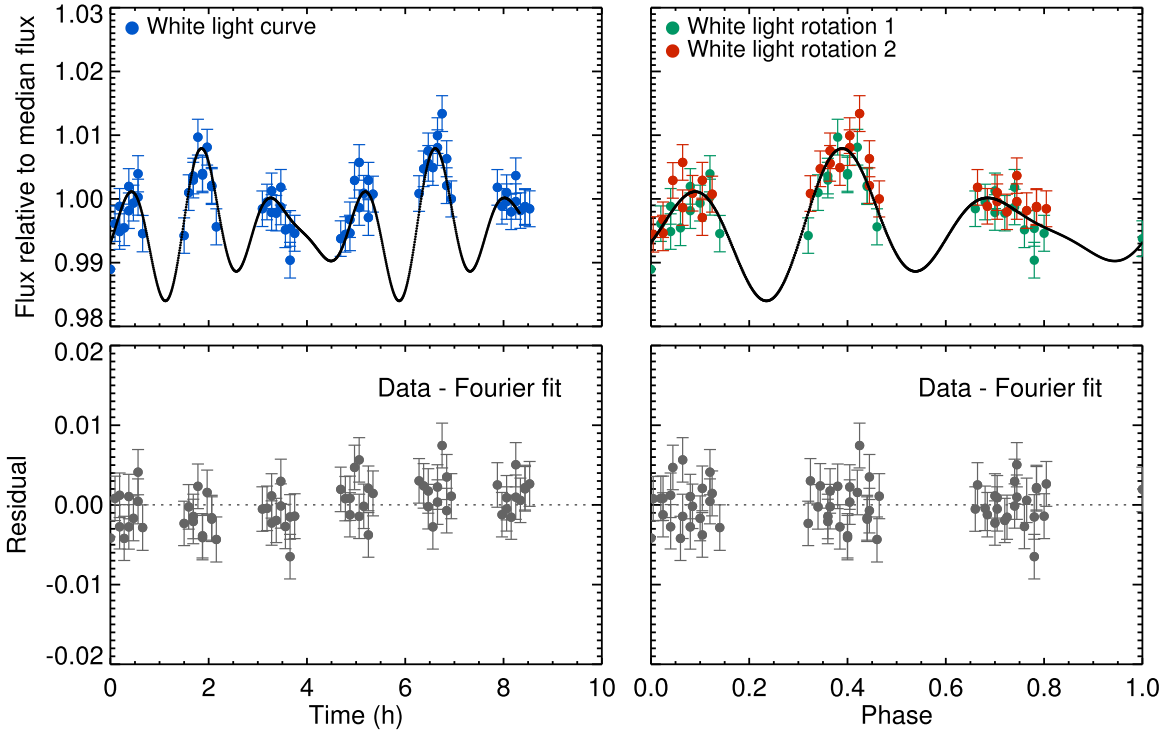
Fourier Component	Value
$P$ (hr)	$4.756 \pm 0.030$
$A_0$	$1.991 \pm 0.002$
$A_1$	$(-1.722 \pm 1.522) \times 10^{-3}$
$B_1$	$(-2.821 \pm 13.653) \times 10^{-4}$
$A_2$	$(5.373 \pm 9.786) \times 10^{-4}$
$B_2$	$(-1.069 \pm 1.085) \times 10^{-3}$
$A_3$	$(2.611 \pm 0.981) \times 10^{-3}$
$B_3$	$(6.372 \pm 1.256) \times 10^{-3}$
$A_4$	$(-3.632 \pm 1.049) \times 10^{-3}$
$B_4$	$(-0.200 \pm 1.052) \times 10^{-3}$

point using a Gaussian random number generator. The mean of the Gaussian is the measured flux of the original light curve, and the standard deviation is the photometric uncertainty of each point. We plotted a combined periodogram, obtained as indicated in Section 6.1.1, of all light curves and overplotted the area between 25% and 75% percentiles in light blue (see Figure 5), and the 50% percentile in a dark blue line. We obtained a main period of  $4.78 \pm 0.95$  hr with a  $5.7\sigma$  detection and a secondary period of  $1.19 \pm 0.06$  hr. The uncertainty on the periods is the FWHM of every of the 50% percentile peak. On the right side plot in Figure 5, we show the distribution of the main period obtained for each of the synthetic light curves created in the Monte Carlo simulation. The solid line represents the mean of the distribution, and the dashed lines represent the  $1\sigma$  of the distribution.

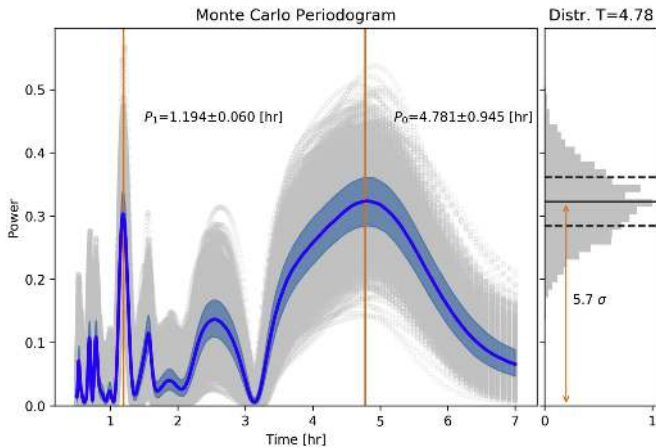
The reason to employ the regular L–S periodogram presented in Section 6.1.1 instead of the BGLS periodogram presented in Section 6.1.2, is that the BGLS normalizes the probabilities of each of the peaks to the maximum peak found in each periodogram for each synthetic light curve. Thus, we are not able to compare the periodograms for different light curves, as the normalization factor changes for each periodogram. The power of the peaks in the regular L–S periodogram are normalized to the variance of the data, which should be quite similar for the synthetic light curves generated in the Monte Carlo simulation. Thus, we can compare the different periodograms for the different synthetic light curves.

2. Prayer Bead Monte Carlo (Moutou et al. 2004; Gillon et al. 2007): this method uses the scatter of the residuals to determine the best model fit, as we obtained in Section 6.1.3. We created 1000 new synthetic light curves, adding the residuals shifted in time by a different random amount and added to the best model light curve. We plotted a combined periodogram, obtained as

4th order Fourier fit

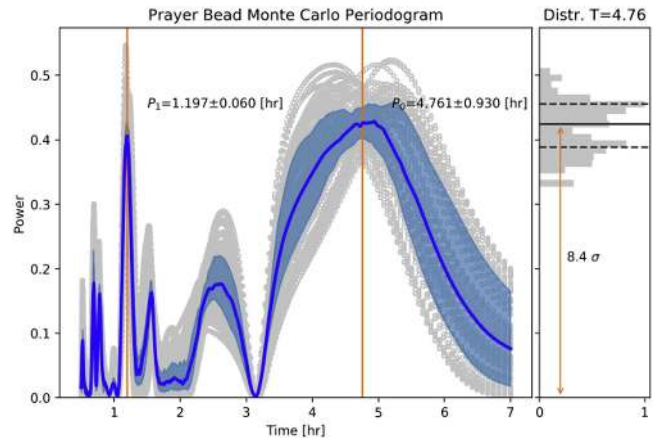


**Figure 4.** Top plots: non-folded light curve of LP261-75B in white light (1.1–1.69  $\mu\text{m}$ ) (left), and folded light curve (right). Overplotted with a black line we show the best fit using a forth-order Fourier function. Bottom plots: residuals after subtracting the best fit with the fourth-order Fourier function from the non-folded and folded white light curves.



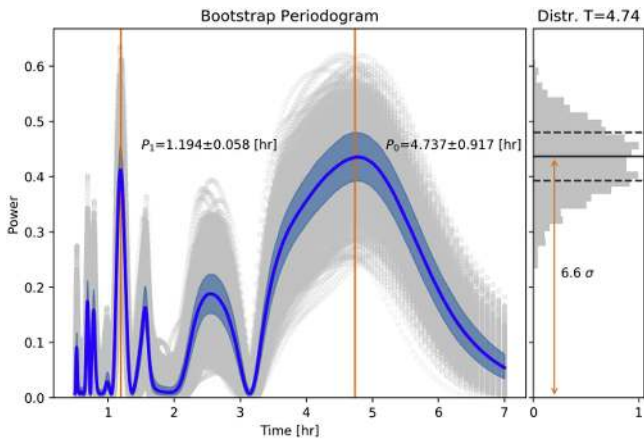
**Figure 5.** Combined periodogram of all the 1000 synthetic white light curves originated in the Regular Monte Carlo simulation. We represent the maximum of the main and secondary peaks with an orange vertical line, that correspond to the two the main and secondary periods found in the Monte Carlo simulation. We overplotted the area between 25% and 75% percentiles in light blue, and the 50% percentile in a dark blue line. In the right side plot, we show the normalized distribution in power of the main period obtained for each of the synthetic light curves created in the Monte Carlo simulation. The solid line represents the mean of the distribution, and the dashed lines represent the  $1\sigma$  of the distribution.

indicated in Section 6.1.1, for the different light curves and overplotted the 25%, 50%, and 75% percentiles using the same color codes as in Figure 6. We obtained a main period of  $4.76 \pm 0.93$  hr with a  $8.4\sigma$  detection, and a secondary period of  $1.20 \pm 0.06$  hr.



**Figure 6.** Combined periodogram of all 1000 synthetic white light curves originated in the Prayer Bead Monte Carlo simulation. The color code is the same as in Figure 5.

3. Bootstrap Monte Carlo: this method is similar to the Prayer Bead Monte Carlo, with the difference that the residuals are randomly permuted and added to the best model light curve, as obtained in 6.1.3, to create each of the new 1000 synthetic light curves. We plotted a combined periodogram, obtained as indicated in 6.1.1, for all light curves and overplotted the 25%, 50%, and 75% percentiles (see Figure 7). We obtained a main period of  $4.74 \pm 0.92$  hr with a  $6.6\sigma$  detection and a secondary period of  $1.19 \pm 0.06$  hr.



**Figure 7.** Combined periodogram of all 1000 synthetic white light curves originated in the Bootstrap Monte Carlo simulation. The color code is the same as in Figure 5.

## 6.2. Spectral Variability

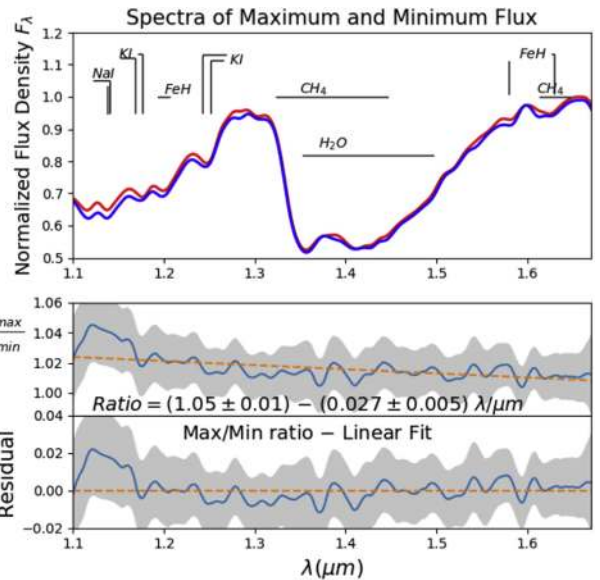
We obtained in total 66 spectra of LP261-75B during six *HST* orbits. We explored the amplitude of the rotational modulations as a function of wavelength by comparing the average of the six spectra with the highest flux and that of the six with lowest flux (Figure 8, top panel). The middle panel of the Figure 8 shows the ratio of the averaged maximum to minimum spectra, i.e., the relative amplitude. The bottom panel shows the result after subtracting a linear fit found for the ratio between the spectra with the maximum and minimum flux of LP261-75B. We found a minimum rotational modulation amplitude of approximately  $2.41\% \pm 0.14\%$  in the average over the entire wavelength range and conclude that the variations are gray, i.e., there is no significant wavelength dependence in the amplitude variations. The amplitudes variations inside the  $\text{H}_2\text{O}$  band ( $1.35\text{--}1.43 \mu\text{m}$ ) and outside the  $\text{H}_2\text{O}$  band are consistent ( $2.80\% \pm 1.02\%$ ).

## 7. Discussion

### 7.1. Rotational Period

All methods presented in Section 6.1 to determine the rotational period of LP261-75B light curve are in statistical agreement, suggesting a main rotational period of  $\sim 4.8$  hr. Nevertheless, it is important to note that our data do not sample the troughs of the light curve. In particular, there are equally spaced gaps in the light curve that result from the *HST*-orbit target-occultation period. This presents a challenge in attempting to reliably determine the LP261-75B rotation period. Contiguous observations over a longer temporal duration (not available from this data set) would more reliably constrain against the possibility of a spurious period determination. Therefore, we adopt as an indicative period, the one obtained in the regular Monte Carlo simulation, ( $4.78 \pm 0.95$  hr), with its more conservative uncertainty.

In addition, based on the fact that many—but not all—continuous brown dwarf light curves show an underlying fundamental period (Metchev et al. 2015; Apai et al. 2017), we could expect that the changes found in the light curve of LP261-75B are at least quasi-periodic. In fact, as the light curves are interpreted as rotational modulations in the literature (see Section 5), this means that they will be periodic or quasi-periodic.



**Figure 8.** Top panel: average of the six maximum (red color) and the six minimum (blue color) spectra of the 66 spectra taken during six *HST* orbits for LP261-75B. Middle panel: ratio between the six spectra with the maximum flux and six spectra with the minimum flux of LP261-75B, with the best linear fit to it. Bottom panel: residuals of the ratio between the six maximum and six minimum spectra of LP261-75B after subtracting the best linear fit.

### 7.2. Spectral Modulations and Cloud Structure

In the spectra of ultracool atmospheres, light of different wavelengths probe different pressure levels. Therefore, spectroscopic rotational modulations inform upon the surface brightness distribution of the atmosphere as functions of longitude and pressure. Spectral contribution functions can be calculated to determine which pressure ranges are probed by which wavelengths. Then, Yang et al. (2016) used state-of-the-art radiative transfer models to evaluate changes in the emerging spectrum in response to changing temperatures in discrete pressure levels to determine the contribution functions. This approach is imperfect, as it does not include readjustment of the cloud cover and atmospheric dynamics in response to the temperature change introduced; nevertheless, it can provide a useful guide for the pressure levels probed for different atmospheres at different wavelengths.

That work (their Figure 16) predicts that for LP261-75B, the *J*-band will probe the highest pressure level in the atmosphere, with 80% of the *J*-band emission emerging from pressures 7 bar and lower. The other continuum band in our study, the *H*-band, probes somewhat shallower depths (pressures 6 bar and lower), while the  $\text{CH}_4\text{--H}_2\text{O}$  ( $1.62\text{--}1.69 \mu\text{m}$ ) molecular band traces the atmosphere 5–6 bar and below. The highest opacity in our wavelength range is in the  $\text{H}_2\text{O}$  ( $1.35\text{--}1.43 \mu\text{m}$ ) band, which probes the atmosphere at pressures  $\sim 4$  bar and lower.

Our measurements allow us to explore atmospheric surface brightness variation *differences* between the 0–4 bar and 0–7 bar pressure ranges. Our time-resolved spectroscopy found nearly flat relative amplitude variations in LP261-75B.

As shown in Figure 8, the observed relative amplitude variations for LP261-75B over the  $1.1\text{--}1.65 \mu\text{m}$  wavelength range have only a slightly descending slope ( $-0.027 \pm 0.005 \mu\text{m}^{-1}$ ). The wavelength dependence of the relative amplitude observed in LP261-75B resembles those reported for two L5 high-gravity brown dwarfs (2MASS J15074769–1627386 and 2MASS J18212815+1414010)



in Yang et al. (2015) and the L6.5-type intermediate surface gravity, extremely red brown dwarf WISEP J004701.06+680352.1 (hereafter W0047). All four L-type objects show nearly linear wavelength dependence in the relative amplitude of the rotational modulations, with very similar relative changes in the  $J$ -band and  $H$ -band continuum and the  $1.4\ \mu\text{m}$  water bands. Only W0047—the highest-amplitude and also reddest object in the sample—shows evidence for a somewhat lower modulation amplitude in the water band.

This pattern stands in stark contrast with the sample of L/T transition dwarfs observed with *HST*: the T2 dwarfs (2MASS J01365662+0933473 and 2MASS J21392676+0220226 in Apai et al. 2013; and 2MASS J10491891-5319100 or Luhman 16B in Buenzli et al. 2015) show greatly reduced modulations in the water band with respect to the modulations observed in the  $J$ -band and  $H$ -band continuum bands.

The amplitudes of the relative modulations argue for a prominent difference between the pressure levels where modulations are introduced, likely through cloud heterogeneities. The fact that there is only small (often undetectable) relative amplitude difference between the water and continuum in L5 dwarfs, argues for the modulation introduced at pressure levels *below* (i.e., higher in the atmosphere) than what are probed in the water band (Yang et al. 2015). This fact, in combination with the observation that the modulations are seen throughout the broad wavelength range of the G141 grism without strong spectral features, led Yang et al. (2015) to argue for the presence of high-altitude, heterogeneous clouds or haze particles in the atmospheres of mid-L-dwarfs.

Our study of LP261-75B provides the fourth mid-L-dwarf with observed spectral modulations across this wavelength range. The fact that LP261-75B shows relative amplitude modulations very similar to the other three mid-L dwarfs demonstrates that particle cover high in the upper atmosphere is a general characteristic of mid-L dwarfs, as was hypothesized by Yang et al. (2015) on the basis of the first two objects. However, there are also important differences: W0047 shows evidence of weak amplitude reduction in the water absorption band and a strong wavelength-dependent amplitude slope, while the three other mid-L-dwarfs (now including LP261-75B) do not. These differences lend further support to the connection between the unusual (extremely red) color of W0047 and its unusual modulations (high-amplitude and with a strong slope), as proposed by Lew et al. (2016).

High-altitude small dust grain populations have been proposed previously to explain the red colors and spectra of mid-L-type brown dwarfs. Marocco et al. (2014) studied the (time-averaged) spectrum of the extremely red L7pec-type brown dwarf ULAS 222711004547 and found that its peculiar red color and spectra can be explained by applying a strong reddening slope to an otherwise typical L7-type field brown dwarf spectrum. Hiranaka et al. 2016 has extended this study and presented a systematic comparison of 26 red field brown dwarfs and 26 brown dwarfs with low gravity spectral indicators (spectral types L0–L7). Using a Markov Chain Monte Carlo-based analysis, they successfully fitted the objects with combinations of spectral standards and haze (modeled as Mie-scattering particles with smooth power-law particle size distributions). Their fits required grains with  $<0.5\ \mu\text{m}$  diameters. The analysis of the posterior probability distributions of the haze parameters demonstrated a difference in particle size distributions between the field brown dwarfs and

the low gravity brown dwarfs, suggesting a gravity dependence in the processes that form or regulate the hazes.

Our findings provide a strong, independent support to this picture: the time-resolved observations allow us to compare opacity variations within *individual* objects, a powerful way to isolate the effects of atmospheric opacity changes from other effects (surface gravity, abundance, vertical mixing) that may be important when comparing different objects to each other. Our observations directly probe the opacity differences without the complicating effects of changes in bulk parameters and also help determine the pressure levels where the small particles must be present.

### 7.3. Interpretation of the LP621-75B Light Curve

Previous mapping efforts of brown dwarf atmospheres using observed light curves showed that a number of cloud heterogeneities, hereafter “spot”, with different sizes and at different locations on the disk can reproduce the observed light curve modulations (Apai et al. 2013; Karalidi et al. 2015). However, the light curve of LP261-75B poses a challenge for the standard mapping techniques, as it is physically unlikely that isolated spots cause the posited three-peaked light curve.

In fact, the light curve appears to be, on the face of it, impossible to explain with a rotating brown dwarf with brightness markings. To understand this, we follow Cowan et al. (2017) in adopting the formalism of Fourier analysis, where  $n = 1$  denotes the fundamental mode (the brown dwarf’s rotational period) and the harmonics are denoted by  $n = 2, 3$ , etc. The amplitudes of each of the Fourier frequencies are:  $\tilde{A}_n = \sqrt{A_n^2 + B_n^2}$  where  $A_n$  and  $B_n$  are the amplitudes in Table 2. If its rotational period is 4.8 hr, then the light curve of LP261-75B is dominated by the  $n = 3$  term, namely three peaks per rotation. We denote the amplitude at this frequency as  $\tilde{A}_3$ ; what we report in practice is the amplitude normalized by the time-averaged flux of the brown dwarf,  $\tilde{A}_0 = A_0/2$ . For the current light curve,  $\tilde{A}_1/\tilde{A}_0 \approx 1.7 \times 10^{-3}$  and  $\tilde{A}_3/\tilde{A}_0 \approx 6.9 \times 10^{-3}$ .

It is intuitive to imagine that three bright spots equally spaced in longitude could produce the light curve of LP261-75B, but that is incorrect: such a map would in fact produce  $\tilde{A}_3 = 0$ . In truth, it has been shown analytically that a rotating brown dwarf seen from an equatorial viewpoint or with a N–S symmetric map cannot produce non- $\tilde{A}_3$  (Cowan & Agol 2008; Cowan et al. 2013)—the so-called “odd nullspace”.

Cowan et al. (2013) showed that the only way to get non-zero odd harmonics in a rotational light curve is with a N–S asymmetric map *and* an inclined viewing geometry. The very simplest map that can produce  $\tilde{A}_3$  is the  $Y_4^3$  spherical harmonic, but one can achieve a similar effect with six spots (three each in the northern and southern hemispheres, offset in longitude).

Spot-based maps tend to produce more power in  $n = 1$  than in  $n = 3$ . Therefore, they may not be able to reproduce our triple-humped light curve. The map–light curve convolution is a low-pass filter, so higher-order harmonics should be strongly suppressed (Cowan & Agol 2008). A corollary of this low-pass filter is that it is difficult to construct a spot-based map that produces significant  $\tilde{A}_3$  without producing at least as much  $\tilde{A}_1$  (Cowan et al. 2017), which is inconsistent with the measured amplitudes of LP261-75B ( $\tilde{A}_3/\tilde{A}_1 \approx 4$ ).

We instead explore whether one could explain the light curve of LP261-75B with a smoothly varying brightness map. In particular, spherical harmonic maps have the advantage of

inducing sinusoidal brightness variations at a single frequency: a  $Y_l^m$  can only produce power at the  $n = m$  harmonic. Following Cowan et al. (2013), a pure  $Y_0^0 + C_4^3 Y_4^3$  map with 13% semi-amplitude could produce  $\tilde{A}_3$  of 1% if the BD is inclined  $60^\circ$  from pole-on. So the light curve of LP261-75B can indeed be produced by a positive map, provided it is fairly smooth. Because the light-curve morphology has not yet been firmly established, we limit ourselves to this existence proof and leave more detailed mapping exercises for the future.

We acknowledge that the phase-folded light curve does not sample, or closely flank, the troughs and that the inferred period is a multiple of the sampling period. To confirm the period found, continuous data coverage with a longer baseline is needed.

## 8. Conclusions



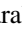





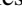

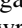
We present six consecutive orbit *HST*/WFC3/G141 time-resolved spectroscopy observations of the LP261-75B brown dwarf, an L6-type wide companion (380 au projected separation) to an M4.5 star. The key findings of our study are as follows.

1. We have discovered rotational modulations in the spectrum of LP261-75B, the fourth variable L-dwarf for which time-resolved spectroscopy has been obtained.
2. We detected a rotational modulation with an amplitude of at least  $2.41\% \pm 0.14\%$  in the 1.1–1.69  $\mu\text{m}$  wavelength range.
3. Based on extensive frequency analysis, we adopted an indicative rotational period of  $4.78 \pm 0.95$  hr for LP261-75B. Due to the incomplete time coverage of the data and the fact that only the peaks of the light curve are sampled, contiguous observations over a longer temporal duration (not available from this data set) would more reliably constrain against the possibility of a spurious period determination.
4. On the basis of the phase-folded light curve, we report a possible triple-peaked light curve. If confirmed, this unusual light curve is most probably generated by longitudinally nearly evenly distributed spots.
5. The ratio of the six maximum and six minimum spectra for LP261-75B is nearly constant across the wavelength range of 1.1–1.69  $\mu\text{m}$ , with a mild slope (larger amplitudes in the blue) and with no measurable decrease in the water absorption band. This finding contributes to the evidence that mid-L dwarfs share a similar rotational modulation trend and lends further support to the proposed high-altitude clouds or hazes in these objects (Yang et al. 2015).

We thank our referee Dr. Derek Homeier for his valuable comments that improved this work. This study is based on observations made with the NASA/ESA *Hubble Space Telescope*, obtained at the Space Telescope Institute, which is operated by AURA, Inc., under NASA contract NAS 5-26555, under GO-14241. This publication makes use of data products from the Two Micron All Sky Survey, which is a joint project of the University of Massachusetts and the Infrared Processing and Analysis Center/California Institute of Technology, funded by the National Aeronautics and Space Administration and the National Science Foundation.

Software: IDL@*periodogram.pro*, *mpfitfun.pro* (Markwardt 2009).

## ORCID iDs

Dániel Apai  <https://orcid.org/0000-0003-3714-5855>  
 Yifan Zhou  <https://orcid.org/0000-0003-2969-6040>  
 Theodora Karalidi  <https://orcid.org/0000-0001-7356-6652>  
 Ben W. P. Lew  <https://orcid.org/0000-0003-1487-6452>  
 Glenn Schneider  <https://orcid.org/0000-0002-4511-5966>  
 Nicolas Cowan  <https://orcid.org/0000-0001-6129-5699>  
 Stan Metchev  <https://orcid.org/0000-0003-3050-8203>  
 Paulo A. Miles-Páez  <https://orcid.org/0000-0003-2446-8882>  
 Adam J. Burgasser  <https://orcid.org/0000-0002-6523-9536>  
 Patrick J. Lowrance  <https://orcid.org/0000-0001-8014-0270>  
 Mark S. Marley  <https://orcid.org/0000-0002-5251-2943>

## References

- Ackerman, A. S., & Marley, M. S. 2001, *ApJ*, 556, 872  
 Allers, K. N., & Liu, M. C. 2007, in AAS Meeting 211 Abstracts, 103.15  
 Apai, D., Karalidi, T., Marley, M. S., et al. 2017, *Sci*, 357, 683  
 Apai, D., Pascucci, I., Bouwman, J., et al. 2005, *Sci*, 310, 834  
 Apai, D., Radigan, J., Buenzli, E., et al. 2013, *ApJ*, 768, 121  
 Artigau, É., Bouchard, S., Doyon, R., & Lafrenière, D. 2009, *ApJ*, 701, 1534  
 Artigau, É., Gagné, J., Faherty, J., et al. 2015, *ApJ*, 806, 254  
 Bailer-Jones, C. A. L., & Mundt, R. 1999, *A&A*, 348, 800  
 Bailer-Jones, C. A. L., & Mundt, R. 2001, *A&A*, 367, 218  
 Brethorst, G. L. 2001, in AIP Conf. Ser. 568, Bayesian Inference and Maximum Entropy Methods in Science and Engineering, ed. A. Mohammad-Djafari (Melville, NY: AIP), 246  
 Buenzli, E., Apai, D., Radigan, J., Reid, I. N., & Flateau, D. 2014, *ApJ*, 782, 77  
 Buenzli, E., Saumon, D., Marley, M. S., et al. 2015, *ApJ*, 798, 127  
 Burgasser, A. J., Kirkpatrick, J. D., & Lowrance, P. J. 2005, *AJ*, 129, 2849  
 Burrows, A., Hubbard, W. B., Lunine, J. I., & Liebert, J. 2001, *RvMP*, 73, 719  
 Carpenter, J. M., Mamajek, E. E., Hillenbrand, L. A., & Meyer, M. R. 2006, *ApJL*, 651, L49  
 Cowan, N. B., & Agol, E. 2008, *ApJL*, 678, L129  
 Cowan, N. B., Chayes, V., Bouffard, É., Meynig, M., & Haggard, H. M. 2017, *MNRAS*, 467, 747  
 Cowan, N. B., Fuentes, P. A., & Haggard, H. M. 2013, *MNRAS*, 434, 2465  
 Cruz, K. L., Kirkpatrick, J. D., & Burgasser, A. J. 2009, *AJ*, 137, 3345  
 Cumming, A., Marcy, G. W., & Butler, R. P. 1999, *ApJ*, 526, 890  
 Dupuy, T. J., & Liu, M. C. 2012, *ApJS*, 201, 19  
 Faherty, J. K., Rice, E. L., Cruz, K. L., Mamajek, E. E., & Núñez, A. 2013, *AJ*, 145, 2  
 Ferraz-Mello, S. 1981, *AJ*, 86, 619  
 Gelino, C. R., Marley, M. S., Holtzman, J. A., Ackerman, A. S., & Lodders, K. 2002, *ApJ*, 577, 433  
 Gillon, M., Demory, B.-O., Barman, T., et al. 2007, *A&A*, 471, L51  
 Gillon, M., Triard, A. H. M. J., Jehin, E., et al. 2013, *A&A*, 555, L5  
 Hiranaka, K., Cruz, K. L., Douglas, S. T., Marley, M. S., & Baldassare, V. F. 2016, *ApJ*, 830, 96  
 Home, J. H., & Baliunas, S. L. 1986, *ApJ*, 302, 757  
 Karalidi, T., Apai, D., Schneider, G., Hanson, J. R., & Pasachoff, J. M. 2015, *ApJ*, 814, 65  
 Kirkpatrick, J. D., Looper, D. L., Burgasser, A. J., et al. 2010, *ApJS*, 190, 100  
 Kirkpatrick, J. D., Reid, I. N., Liebert, J., et al. 2000, *AJ*, 120, 447  
 Knutson, H. A., Charbonneau, D., Allen, L. E., et al. 2007, *Natur*, 447, 183  
 Koen, C. 2003, *MNRAS*, 346, 473  
 Lew, B. W. P., Apai, D., Zhou, Y., et al. 2016, *ApJL*, 829, L32  
 Liddle, A. R. 2007, *MNRAS*, 377, L74  
 Liu, M. C., Dupuy, T. J., & Allers, K. N. 2016, *ApJ*, 833, 96  
 Lomb, N. R. 1976, *Ap&SS*, 39, 447  
 MacKenty, J. W., Kimble, R. A., O'Connell, R. W., & Townsend, J. A. 2010, *Proc. SPIE*, 7731, 77310Z  
 Markwardt, C. B. 2009, in ASP Conf. Ser. 411, Astronomical Data Analysis Software and Systems XVIII, ed. D. A. Bohlender, D. Durand, & P. Dowler (San Francisco, CA: ASP), 251  
 Marocco, F., Day-Jones, A. C., Lucas, P. W., et al. 2014, *MNRAS*, 439, 372  
 Metchev, S. A., Heinze, A., Apai, D., et al. 2015, *ApJ*, 799, 154  
 Miles-Páez, P. A., Metchev, S. A., Heinze, A., & Apai, D. 2017, *ApJ*, 840, 83

- Morales-Calderón, M., Stauffer, J. R., Kirkpatrick, J. D., et al. 2006, *ApJ*, 653, 1454
- Mortier, A., Faria, J. P., Correia, C. M., Santerne, A., & Santos, N. C. 2015, *A&A*, 573, A101
- Moutou, C., Pont, F., Bouchy, F., & Mayor, M. 2004, *A&A*, 424, L31
- Pascucci, I., Apai, D., Luhman, K., et al. 2009, *ApJ*, 696, 143
- Radigan, J., Jayawardhana, R., Lafrenière, D., et al. 2012, *ApJ*, 750, 105
- Reid, I. N., Cruz, K. L., Burgasser, A. J., & Liu, M. C. 2008, *AJ*, 135, 580
- Reid, I. N., & Walkowicz, L. M. 2006, *PASP*, 118, 671
- Saumon, D., & Marley, M. S. 2008, *ApJ*, 689, 1327
- Scargle, J. D. 1982, *ApJ*, 263, 835
- Shkolnik, E., Liu, M. C., & Reid, I. N. 2009, *ApJ*, 699, 649
- Simon, A. A., Rowe, J. F., Gaulme, P., et al. 2016, *ApJ*, 817, 162
- Stauffer, J. R., Schild, R., Barrado y Navascués, D., et al. 1998, *ApJ*, 504, 805
- Tinney, C. G., & Tolley, A. J. 1999, *MNRAS*, 304, 119
- Yang, H., Apai, D., Marley, M. S., et al. 2015, *ApJL*, 798, L13
- Yang, H., Apai, D., Marley, M. S., et al. 2016, *ApJ*, 826, 8
- Zechmeister, M., & Kürster, M. 2009, *A&A*, 496, 577
- Zhou, Y., Apai, D., Lew, B. W. P., & Schneider, G. 2017, *AJ*, 153, 243